

# 1 Measuring Mass-Based Hygroscopicity of 2 Atmospheric Particles through *in situ* Imaging

3 *Dominique S. Piens*,<sup>1,#,\*</sup> *Stephen T. Kelly*,<sup>1,%</sup> *Tristan H. Harder*,<sup>1,2</sup> *Markus D. Petters*,<sup>3</sup> *Rachel E.*  
4 *O'Brien*,<sup>1,&</sup> *Bingbing Wang*,<sup>4,^</sup> *Ken Teske*,<sup>5</sup> *Pat Dowell*,<sup>5</sup> *Alexander Laskin*,<sup>4</sup> *Mary K. Gilles*<sup>1,\*</sup>

5 <sup>1</sup>Chemical Sciences Division, Lawrence Berkeley National Laboratory, Berkeley, California  
6 94720, USA

7 <sup>2</sup>Department of Chemistry, University of California, Berkeley, California 94720, USA

8 <sup>3</sup>Department of Marine Earth and Atmospheric Sciences, North Carolina State University,  
9 Raleigh, North Carolina 27695, USA

10 <sup>4</sup>William R. Wiley Environmental and Molecular Sciences Laboratory, Pacific Northwest  
11 National Laboratory, Richland, Washington 99352, USA

12 <sup>5</sup>Atmospheric Radiation Monitoring (Southern Great Plains Climate Research Facility), 109596  
13 Coal Road, Billings, Oklahoma 74630 USA

14

15 \*email: [dpiens@stanford.edu](mailto:dpiens@stanford.edu), [mkgilles@lbl.gov](mailto:mkgilles@lbl.gov)

16 #Present address: Stanford University, Stanford, California 94305, USA

17 %Present address: Carl Zeiss X-ray Microscopy Inc., Pleasanton, California 94588 USA

18 &Present address: Department of Civil and Environmental Engineering, Massachusetts Institute of Technology,  
19 Cambridge, Massachusetts 02139, USA

20 ^Present address: State Key Laboratory of Marine Environmental Science, College of Ocean and Earth Sciences,  
21 Xiamen University, Xiamen 361102, China

22

23

24 Keywords: aerosol water uptake, hygroscopic growth, scanning transmission X-ray microscopy,  
25 STXM, Southern Great Plains, NaCl, NaBr, (NH<sub>4</sub>)<sub>2</sub>SO<sub>4</sub>, KCl, fructose, levoglucosan  
26 deliquescence, atmospheric aerosols, single particle, mass-based hygroscopic growth, in situ,

27 *Manuscript in preparation for*

28 *Environmental Science and Technology*

29

30

31 **ABSTRACT**

32 Quantifying how atmospheric particles interact with water vapor is critical for  
33 understanding the effects of aerosols on climate. We present a novel method to measure the  
34 mass-based hygroscopicity of particles while characterizing their elemental and carbon  
35 functional group compositions. Since mass-based hygroscopicity is insensitive to particle  
36 geometry, it is advantageous for probing the hygroscopic behavior of atmospheric particles,  
37 which can have irregular morphologies. Combining scanning electron microscopy with energy  
38 dispersive X-ray analysis (SEM/EDX), scanning transmission X-ray microscopy (STXM)  
39 analysis, and *in situ* STXM humidification experiments, this method was validated using  
40 laboratory-generated, atmospherically relevant particles. Then, the hygroscopicity and elemental  
41 composition of 15 complex atmospheric particles were analyzed by leveraging quantification of  
42 C, N, and O from STXM, and complementary elemental quantification from SEM/EDX. We  
43 found three types of hygroscopic responses, and correlated high hygroscopicity with Na and Cl  
44 content. The mixing state of 158 other particles from the sample broadly agreed with those of the  
45 humidified particles, indicating the potential to infer atmospheric hygroscopic behavior from a  
46 selected subset of particles. These methods offer unique quantitative capabilities to characterize  
47 and correlate the hygroscopicity and chemistry of individual submicron atmospheric particles.

## 48 INTRODUCTION

49 Atmospheric aerosols affect the Earth's climate through direct effects, such as scattering  
50 and absorbing incident sunlight, and through indirect effects, where atmospheric particles  
51 interact with water vapor and act as cloud condensation or ice nuclei.<sup>1</sup> Their hygroscopic  
52 properties feedback with the uptake of volatile organics, and ultimately affect the atmospheric  
53 evolution and lifetime of particles. Quantifying how an airborne particle interacts with water  
54 vapor is critical for predicting the effect of particles on the atmospheric environment and climate,  
55 and remains an important challenge.

56 Multiple techniques that characterize the hygroscopic behavior of particles with precision  
57 focus on either single-particle size measurements or the effect of water vapor on an ensemble of  
58 airborne particles.<sup>2,3</sup> Frequently, in field measurements, hygroscopic tandem differential mobility  
59 analysis (HTDMA) is used to measure particle hygroscopicity.<sup>4,6</sup> With HTDMA, hygroscopic  
60 growth is quantified from changes in particle size as a function of relative humidity. However,  
61 quantifying hygroscopic growth using size is susceptible to errors due to particle asphericity and  
62 particle porosity. Additionally, inferring the hygroscopic growth of internally mixed aerosols  
63 from that of their constituent compounds using size may be limited by non-ideal volume  
64 additivity. Mass-based hygroscopic growth measurement provides an alternate and  
65 complimentary method to quantify water uptake.

66 The extent of water uptake, detailed microstructural changes of individual particles  
67 deposited on substrates, and correlation of microstructural changes with particle composition  
68 and/or chemistry during hydration/dehydration cycling can be investigated with  
69 spectromicroscopy. Spectromicroscopic methods include micro-FTIR,<sup>7,8</sup> micro-Raman,<sup>9-11</sup>  
70 micro-Raman combined with atomic force microscopy,<sup>12</sup> scanning and transmission electron

71 microscopy with energy dispersive analysis of X-rays (SEM/EDX and TEM/EDX,  
72 respectively),<sup>13-18</sup> and scanning transmission X-ray microscopy with near-edge X-ray absorption  
73 fine structure spectroscopy (STXM/NEXAFS).<sup>19</sup> These are used to examine particle  
74 efflorescence and deliquescence,<sup>20</sup> changes in morphology,<sup>21</sup> water vapor uptake,<sup>22</sup> and liquid-  
75 liquid phase separation.<sup>23-25</sup> STXM/NEXAFS measures optical absorption, which is proportional  
76 to mass, with high precision, both spatially and energetically resolved. STXM/NEXAFS is  
77 uniquely capable of quantitative analysis of the light elements (C, N, O) while probing their  
78 chemical bonding at spatial resolution down to 25 nm.<sup>19,26-28</sup> Several groups have employed  
79 chemical imaging by STXM/NEXAFS under controlled water vapor environment.<sup>21,29-33</sup> These  
80 include qualitative observations of hygroscopic properties in humic like substances (HULIS) as  
81 proxies for aerosols,<sup>33</sup> atmospheric particles collected from the Amazonian basin,<sup>21</sup> deliquescence  
82 and efflorescence of laboratory generated particles,<sup>30,32</sup> and quantitative measurements of water  
83 content in single-component proxies of atmospheric particles.<sup>29,34</sup> Mikhailov et.al. combined  
84 STXM/NEXAFS and electron microscopy (transmission mode) humidification experiments to  
85 investigate hygroscopicity of field-collected atmospheric aerosols.<sup>35</sup> Quantification of the mass-  
86 based hygroscopicity was done using filter samples with a differential hygroscopicity analyzer  
87 (FDHA). However, quantification of mass-based hygroscopicity for individual particles was not  
88 performed.

89         Here, a methodology is presented to quantify mass-based water uptake in individual  
90 submicron particles that combines STXM/NEXAFS particle characterization with *in situ* and  
91 water vapor uptake measurements complemented with subsequent SEM/EDX elemental  
92 composition microanalysis. The utility of *in situ* STXM/NEXAFS chemical imaging for mass-  
93 based water vapor uptake measurements is demonstrated using laboratory-generated particles of

94 known compositions and uniform morphologies. Field samples, collected from the Department  
95 of Energy's Atmospheric Radiation Monitoring (DOE-ARM) site in the Southern Great Plains  
96 (SGP) field site, are then examined. First, dry characterization of the particles was done using  
97 STXM/NEXAFS, then in situ water vapor uptake experiments were performed using  
98 STXM/NEXAFS. Subsequently, SEM/EDX elemental characterization of the identical particles  
99 was performed. Finally, a composition analysis combined the STXM/NEXAFS and SEM/EDX  
100 data sets to determine mass-based hygroscopicity parameters for the atmospheric particles  
101 collected at the SGP site. This study is the first application combining STXM/NEXAFS and  
102 SEM/EDX to determine total mass of individual particles before and during hygroscopic growth  
103 both for the laboratory generated as well as field samples. The use of mass rather than size to  
104 track hygroscopic growth enabled the extension of established methods to atmospheric particles.  
105 A brief discussion on the future outlook for utilizing this analysis to extract mass-based  
106 hygroscopicity parameters from any complex heterogeneous population of atmospheric particles  
107 is presented.

## 108 **EXPERIMENTAL SECTION**

109 **Laboratory Particle Preparation.** Particles composed of NaCl, NaBr,  $(\text{NH}_4)_2\text{SO}_4$ , KCl,  
110 fructose, and levoglucosan were prepared by nebulizing (nebulizer, Stalter Labs, model 8900) a  
111 dilute solution (0.5 M) of stock chemical in deionized  $\text{H}_2\text{O}$  (18  $\text{M}\Omega$  cm resistivity). Particles then  
112 passed through a diffusion dryer, and were collected onto  $\text{Si}_3\text{N}_4$  substrates on the 7<sup>th</sup> stage ( $D_{50} =$   
113  $0.56 \mu\text{m}$ ) of a Multi-Orifice Uniform Deposition Impactor (MOUDI; model 110-R, MSP, Inc.).  
114 To dry and recrystallize the particles, the substrates were baked at  $\sim 80^\circ\text{C}$  in ambient atmosphere  
115 for several days and then stored in a desiccator until use (several days-months).

116           **Atmospheric Particle Collection.** Atmospheric particles were collected at the DOE-  
117 ARM SGP sampling site in Oklahoma, USA on March 27<sup>th</sup> 2014 at 19:00 GMT. Particle samples  
118 were collected for 20 minutes using a 4-stage Sioutas cascade impactor operated at a flow rate of  
119 9 L/min. Each stage was preloaded with silicon nitride membrane substrates ( $0.5 \times 0.5 \text{ mm}^2$   
120  $\text{Si}_3\text{N}_4$  window size, 100 nm membrane thickness,  $5 \times 5 \text{ mm}^2$  Si frame size; Silson, Inc.) and  
121 filmed TEM grids (Carbon type B film, Copper 400 mesh grids; Ted Pella, Inc.). To ensure that  
122 the samples were within the linear range of Beer's law for absorption, particles collected on the  
123 fourth stage ( $D_{50} = 0.25 \mu\text{m}$ ) were used for microscopy analysis. After collection, the samples  
124 were placed in sealed containers, transported, and then stored in a desiccator (20-30 % relative  
125 humidity) until STXM analysis (two weeks later). Between subsequent experiments (water vapor  
126 uptake, SEM/EDX, additional STXM analysis) over the following 6 months, the samples were  
127 stored in a sealed package in a desiccator.

128           **STXM/NEXAFS Measurements.** STXM/NEXAFS was used to characterize the dry  
129 laboratory and field samples. The measurements were performed at beamline 11.0.2 of the  
130 Advanced Light Source at Lawrence Berkeley National Laboratory. Details of the STXM  
131 instrument and its operation are described elsewhere,<sup>36</sup> its applications for analysis of  
132 atmospheric particles are described in a recent review,<sup>19</sup> and additional details on these  
133 experiments as well as nitrogen analysis are included in the Supporting Information (SI) file.  
134 Briefly, in STXM experiments, monochromatic light from the synchrotron is focused to a small  
135 (25-40 nm) spot at the sample location by a Fresnel zone plate lens. The sample is raster scanned  
136 through the focused beam while the transmitted X-rays are collected on a single element detector  
137 behind the sample to create an image. By changing the X-ray energy, the image contrast can be  
138 changed to highlight particular molecular bonds and functional groups. Absorption at a given X-

139 ray energy is proportional, among other factors, to the mass and composition of the matter in the  
140 X-rays' path. Collecting the same image at different X-ray energies spanning across an elemental  
141 absorption (referred to collectively as a *stack*) allows data acquisition for spatially resolved  
142 NEXAFS spectroscopy. Specific energies are then selected to acquire “short stacks” at a reduced  
143 number of energies. These “short stacks” allow more rapid mapping of carbon functional groups  
144 to allow data acquisition on a larger number of particles within the limited beamtime. Here, the  
145 number of data points collected at the C, N, and O pre-edge and post-edge energies is larger than  
146 previously used.<sup>37</sup> In samples containing a significant fraction of inorganic constituents, this  
147 allows a more precise fitting of the fall off of the absorption cross section, using the Henke  
148 functions<sup>38</sup> to constrain the inorganic mass. The presence of an element is quantitatively *mapped*  
149 by comparing an image collected either in the post-edge region (~25-30 eV beyond the elemental  
150 absorption edge for elemental mapping) or at a particular molecular resonance (to map chemical  
151 bonding) to an image collected in the pre-edge region ~15-20 eV below the energy where the  
152 element absorbs. Additional details are provided in the SI.

153 **Characterization of Laboratory Generated Particles.** Samples of laboratory-generated  
154 particles were directly loaded in the micro reactor used for the water vapor uptake experiments.  
155 Prior to humidification, STXM/NEXAFS oxygen maps of individual dry submicron particles  
156 confirmed the absence of oxygen in NaCl, NaBr, and KCl, laboratory generated samples,  
157 indicating that they were free of water. For these salt particles as well as  $(\text{NH}_4)_2\text{SO}_4$ , carbon data  
158 was not acquired. For fructose and levoglucosan, both carbon short stacks and oxygen maps were  
159 collected prior to water vapor exposure.

160 **Characterization of Particles from the Southern Great Plains.** To ascertain how  
161 representative the particles used for the water vapor uptake experiments were, prior to



162 humidification experiments, 158 additional particles from the field sample were analyzed. The  
163 STXM/NEXAFS stacks of particles from SGP field samples at the carbon K-edge provided  
164 information on their chemical composition and allowed a mixing state classification based on the  
165 amounts of organic carbon (OC),  $sp^2$ -hybridized carbon (an indicator of soot or elemental  
166 carbon, EC), and inorganic species (IN).<sup>37</sup> For the mixing state determination, values for the  
167 optical density across the carbon edge for every pixel allowed an analysis of the chemical  
168 composition on a pixel-by-pixel basis. After analyzing the individual pixels, a compositional  
169 map of each particle was generated. Particles can contain mixtures of the three components:  
170 organic (OC), inorganic (IN), and black carbon/soot (EC). Additional analysis details are  
171 provided in Moffet et al.<sup>37</sup> The STXM particle mixing state was classified as organic carbon  
172 (OC), organic carbon with elemental carbon (OCEC), organic carbon with elemental carbon and  
173 inorganics (OCECIN) or organic carbon with inorganics (OCIN).<sup>37</sup>

174 ***In Situ* STXM/NEXAFS Water Vapor Uptake Measurements.** The micro-reactor,  
175 described in Kelly et al.,<sup>30</sup> was used for *in situ* STXM/NEXAFS chemical imaging of particles  
176 exposed to controlled relative humidity (RH). Two helium gas flows with a combined flow rate  
177 of 6 standard cubic centimeters per minute, one saturated with water vapor and the other dry,  
178 were used to control RH inside the reactor. A sensor (GE Chipcap-L), located in the reactor,  
179 measured RH and temperature inside the reactor. A  $SiN_x$  window with a sample of impacted  
180 particles is mounted to the removable front metal plate using a small amount of wax  
181 (Crystalbond 509, SPI Supplies). Since the wax must be heated to be applied to the  $SiN_x$   
182 window, impacted aerosols are exposed to a maximum temperature of up to 50-70 °C for 15-30  
183 seconds during mounting.

184 After 158 particles were characterized using a higher resolution zone plate (25 nm) for  
185 inorganic content (i.e. L edges for Na, Mg, Cl, S), carbon, and oxygen, the sample was loaded in  
186 the micro reactor for the water vapor uptake experiments. Due to geometrical constraints  
187 discussed in Kelly et al.,<sup>30</sup> the water vapor uptake experiments used a 40 nm Fresnel zone plate.  
188 Visual pattern recognition was used to select three sample regions, containing particles with  
189 compositions and morphologies representative of those in the initial characterization of 158  
190 particles. Based on previous salt deliquescence experiments,<sup>29</sup> we selected regions with sufficient  
191 spacing between particles to limit coalescence during hygroscopic growth. For each of these  
192 regions, carbon short stacks and oxygen maps were collected under dry (<4 % RH) conditions  
193 with 40 nm lateral resolution.

194 The RH was then increased stepwise (steps of 5-10 % RH) and stabilized for 5-10  
195 minutes before each set of data acquisition. At each RH step, oxygen maps (difference between  
196 absorption at the oxygen K-edge pre edge energy, 525 eV, and the post edge at 550 eV) were  
197 collected to quantify changes in the particle oxygen content attributed to water uptake. After  
198 reaching the maximum RH, the RH was decreased (steps of 10-20% RH) and stabilized for 5-10  
199 minutes prior to collecting oxygen maps. The total number of single-energy images acquired on  
200 each region was approximately 120. Hence, the soft X-ray irradiation was minimized and similar  
201 to that typical of a single carbon full stack. Pattern matching with the positions and morphologies  
202 of impacted aerosols allowed rapid relocation of the identical particles for subsequent SEM/EDX  
203 analysis.

204 **SEM/EDX Measurements.** After the STXM/NEXAFS water vapor uptake experiments,  
205 the identical particles were relocated and imaged for elemental composition using SEM/EDX.  
206 An FEI Quanta digital field emission gun environmental scanning electron microscope was used

207 in this work. The microscope is equipped with an EDAX X-ray spectrometer with a Si(Li)  
208 detector with an active area of 10 mm<sup>2</sup> and an ATW2 window. X-ray spectra were acquired for  
209 the same individual particles probed in the STXM experiments for 10 s, at a beam current of 430  
210 pA and an accelerating voltage of 20 kV. Elements considered in the X-ray analysis were Na,  
211 Mg, Al, P, S, Cl, K, Ca, Mn, Fe, and Zn. Individual particle EDX spectra were pre-processed  
212 removing elements having less than 0.5 atomic %. Additional details of the SEM/EDX analysis  
213 of deposited particles are found in Laskin et al.<sup>15</sup> and references therein.

214 **Data Processing and Analysis.** The analytical techniques, applications, and limitations  
215 of the mapping and quantitative chemical imaging of particle samples by STXM are presented  
216 elsewhere<sup>19</sup> and only briefly discussed here. Data analysis is performed using MATLAB  
217 (Mathworks, Natick, MA). Two-dimensional transmission intensity images are obtained by  
218 raster-scanning samples of impacted particles in the STXM. In each image, the background  
219 intensity value ( $I_0$ ) is determined from substrate areas without particles.  $I_0$  is used to convert  
220 transmission intensity into optical density, (OD), using Beer's law. This analysis required  
221 additional MATLAB scripts beyond those in Moffet et al.<sup>37</sup> To identify image areas  
222 corresponding to individual particles, masks were manually drawn around particles. Individual  
223 particles at different RH values were matched visually. For each particle and RH, particle mass,  
224  $m$ , was calculated using

$$225 \quad m = \frac{\sum_i OD_i S}{\mu} \quad (1)$$

226 where  $i$  is a pixel in a particle's image,  $OD_i$  is the absorption at the  $i$ -th pixel at a given X-ray  
227 energy,  $m$  is the particle mass, and  $S$  is the area of a pixel. The particle's mass-absorption cross  
228 section,  $\mu$ , is based on the particle's average elemental composition, and calculated using

$$229 \quad \mu = \frac{\sum_j x_j A_j \mu_j}{\sum_j x_j A_j} \quad (2)$$

230 where  $x_j$  is the atomic fraction of element  $j$ ,  $A_j$  is the molar mass of element  $j$ , and  $\mu_j$  is the mass-  
231 absorption cross section of element  $j$  at the specific X-ray energy.<sup>38</sup> OD at the X-ray energies of  
232 an element's X-ray absorption edge and the mass-absorption cross section of that element are  
233 used in eq. 1 to obtain the mass of a given element in a particle. The parameters in eq 1 and eq 2  
234 are determined experimentally for C, N, and O using STXM/NEXAFS and using SEM/EDX for  
235 most other elements.

236 Dry particle masses (~4% RH) and masses of the particle plus condensed water were  
237 calculated using these formulas and used to derive mass-based growth factors. This step is  
238 analogous to that employed by Ghorai and Tivanski.<sup>29</sup> For laboratory-generated particles  
239 containing oxygen, the dry mass is determined with eq 1 at the oxygen pre-edge using their  
240 known chemical formula. Laboratory-generated aerosols without oxygen (i.e. NaCl and other  
241 salts) were calculated with no dry oxygen mass (confirmed with STXM/NEXAFS imaging). To  
242 obtain the mass of the condensed water, the total oxygen mass was calculated using eq 1 at the  
243 oxygen post-edge. For oxygen-containing particles (fructose, levoglucosan, and ammonium  
244 sulfate), water mass at each RH is obtained by subtracting the initial dry oxygen mass from the  
245 total oxygen mass to obtain the condensed water mass ( $m_w$ ). Dry total mass ( $m_s$ ) and  $m_w$  yield a  
246 mass-based growth factor at every RH ( $g_m$ ).

$$247 \quad g_m = \frac{m_s + m_w}{m_s} \quad (3)$$

248 **Total Masses from STXM/NEXAFS and SEM/EDX: Atmospheric Particles of**  
249 **Unknown Composition.** STXM/NEXAFS measurements of C, N, and O were combined with  
250 the SEM/EDX measurements for high-Z elements to calculate the total mass of dry individual  
251 particles. In STXM/NEXAFS the sum of the OD over all pixels of a given particle is  
252 proportional to the mass-absorption cross section of the average composition of the particle, and

253 to its total mass (eq 1). Total OD for elements other than C, N, and O is obtained by summation  
254 over a particle's STXM/NEXAFS image pixels at 278 eV (the carbon, nitrogen, and oxygen *K*  
255 pre-edges). An empirical formula for the average composition of a particle is obtained by  
256 summing its spatially resolved atomic fractions of the most common elements of Na, Mg, Al, P,  
257 S, Cl, K, Ca, Mn, Fe, and Zn measured with SEM/EDX. SEM/EDX is quantitative<sup>15</sup> for these  
258 elements and they represent the majority of particle inorganic mass. A mass-absorption cross  
259 section, calculated from the empirical formula using eq 2, is used in eq 1 to obtain the total  
260 inorganic mass. Si was excluded because the sample substrate contains silicon. The uncertainty  
261 due to this is discussed in the SI file as well as additional information on the nitrogen content  
262 (Figure S1 and related discussion). Carbon, nitrogen, and oxygen masses obtained from  
263 STXM/NEXAFS were added to the inorganic mass determined with SEM/EDX to obtain the  
264 total mass of each individual dry particle.

## 265 **RESULTS AND DISCUSSION**

### 266 **Hygroscopic Behavior of Laboratory-Generated Samples with Known**

267 **Composition.** In Figure 1, experimental values of the mass-based growth factor ( $g_m$ ) as a  
268 function of RH obtained from STXM/NEXAFS, represented by triangles, are compared to values  
269 predicted by the thermodynamic model AIOMFAC, shown as solid black lines.<sup>39,40</sup> Dashed black  
270 lines indicate the sorption isotherm of idealized crystalline salts. Prior to deliquescence,  
271 hygroscopic growth is negligible. At deliquescence, hygroscopic growth appears as a step to the  
272  $g_m$ , as predicted by AIOMFAC. Data on the mass-based growth factors for laboratory generated  
273 samples as a function of relative humidity are provided in the Supporting Information Tables S1-  
274 S4.

275 Generally, the salts (Fig. 1 a-d) follow idealized crystalline growth until their  
276 deliquescence RH (DRH), and after their DRH, agree with AIOMFAC. KCl (Fig. 1c) and  
277 ammonium sulfate (Fig. 1d) further support that trend in hygroscopic behavior because the  
278 hysteresis during their dehydration resembles the growth of aqueous particles modeled by  
279 AIOMFAC. Due to limited instrumental access, values for  $g_m$  were not obtained during  
280 dehydration for the other lab-generated samples or above DRH. The DRH observed for NaBr is  
281 consistent with those reported by Cohen et al. (between 44.5% and 45.5%)<sup>41</sup> and Wise et al.  
282 (between 46% and 47%)<sup>18</sup>. For NaBr, the value of  $g_m$  jumps from 1.1 at 47% RH to 1.6 at 49%  
283 RH. Within the RH measurement uncertainty of 2%<sup>30</sup> the measured DRH of the crystalline salts  
284 are in agreement with literature values.

285 Unlike crystalline salts, which exhibit sharp deliquescence phase transition, levoglucosan  
286 and fructose exhibit gradual hygroscopic growth. Similar differences between experimental and  
287 theoretical growth factors for levoglucosan were observed by Mikhailov et al.<sup>42</sup> and Mochida and  
288 Kawamura.<sup>43</sup> Measured levoglucosan  $g_m$  values increase more rapidly with higher RH than a  
289 UNIFAC-based model predicts. AIOMFAC uses UNIFAC group contribution methods to predict  
290 activity coefficients and hygroscopic behavior. Mochida and Kawamura<sup>43</sup> proposed that  
291 UNIFAC interaction coefficients were not optimized for organic molecules containing a high  
292 ratio of polar groups to nonpolar groups or closely-spaced polar groups such as levoglucosan.  
293 The sorption isotherm for fructose also exhibits higher growth at high RH than predicted by  
294 AIOMFAC.

295 The difference between AIOMFAC and experimental values could partially be explained  
296 by a combination of our methods estimating lower initial particle mass and higher water mass at  
297 high RH than AIOMFAC. Given their continuing hygroscopic growth, sugar particles were

298 amorphous rather than crystalline. Although the sugar particles were gently dried at 80°C over  
299 several hours or overnight, they may have contained trace residual water and been highly  
300 viscous. Mikhailov et al. suggested that this scenario could lead to higher observed  $g_m$  values at  
301 high RH since the observed initial particle mass will be lower than the theoretical one due to  
302 water adsorption being surface limited.<sup>42</sup> Therefore, differences between model assumptions and  
303 experimental conditions could explain some of the deviations in the  $g_m$  of sugars at high RH  
304 between experiment and AIOMFAC. Future experiments measuring the hygroscopic growth of  
305 lab-generated organic particles containing traces of inorganics would approximate atmospheric  
306 particles more closely, and reveal how differences between AIOMFAC and experiment impact  
307 our methods for atmospheric particles. Overall, these methods measure the hygroscopic response  
308 of individual particles of known composition in agreement with AIOMFAC.

### 309 **Hygroscopic Behavior of Atmospheric Aerosol Samples of Unknown Composition.**

310 This is the first time STXM/NEXAFS and SEM/EDX are combined to determine mass-  
311 based growth factors for field collected atmospheric particles. This combination leverages the  
312 strengths of each technique and enables accurate determination of particle mass and adsorbed  
313 water mass, while also spatially identifying prominent organic chemical functional groups within  
314 individual particles.

315 Figure 2 depicts the range of characteristic hygroscopic curves measured for complex  
316 individual atmospheric particles containing both organic and inorganic components. Particles  
317 cluster into three types of hygroscopic responses labeled as low, medium, and high  
318 hygroscopicity particles. Mass-based growth factors as a function of relative humidity for these  
319 three types are provided in the Supporting Information Tables S5-S7.

320 The size-based growth factors of the atmospheric particles (Figure S2 and Table S9,  
321 Supporting Information) yield very different growth curves. In contrast to mass-based  
322 hygroscopic growth, the particles do not cluster by type based on size growth factors obtained  
323 from their area equivalent diameter. Additionally, the 2D projections for some particles even  
324 decrease with increased water uptake, likely due to recrystallization and mechanical  
325 rearrangement as observed by Kramer et al. (1999).<sup>44</sup> Hence, the findings in this manuscript are  
326 only observable with its transmission imaging techniques using mass-based growth factors rather  
327 than size-based growth factors.

328 Complementary, STXM/NEXAFS can quantify C, N, and O content and water uptake,  
329 while SEM/EDX can quantify inorganic elements on a single-particle basis. Figure 3 shows  
330 atomic fractions of inorganic elements for low, medium, and high hygroscopicity particles. A  
331 single correlation was found between the composition of the inorganic fraction of particles and  
332 the hygroscopic response of particles. High hygroscopicity particles have higher atomic fractions  
333 of Na and Cl than medium and low hygroscopicity particles. The range from one standard  
334 deviation below to one standard deviation above the mean Na fraction of high hygroscopicity  
335 particles is higher than and does not overlap with the same ranges for medium and low  
336 hygroscopicity particles. The trend is similar for Cl fractions, though there is some overlap  
337 between the lower range for high hygroscopicity particles and the upper range for low  
338 hygroscopicity particles. The water sorption isotherm of lab-generated NaCl is shown with the  
339 water sorption isotherm of the high hygroscopicity particles in Figure 2. The plot emphasizes  
340 that high hygroscopic growth occurs between 72% and 78% RH for high hygroscopicity  
341 particles, very near NaCl DRH (75.3% RH). Laboratory-generated NaCl and high hygroscopicity  
342 particles have similar discontinuities in hygroscopic growth. This suggests that Na and Cl in the



343 form of NaCl may drive the hygroscopic growth of high hygroscopicity particles. Atomic  
344 fractions for the other elements show significant overlap between particles with different  
345 hygroscopicities.

346 To provide an alternate representation of the hygroscopicity of the atmospheric particles,  
347 another parameter representing aerosol-water interactions is presented in Figure 3. Petters and  
348 Kreidenweis introduced the use of a single parameter,  $\kappa$ , to represent the effect a particle has on  
349 water activity by calculating the ratio of the volume of water to particulate matter.<sup>42</sup> Higher  
350 values of  $\kappa$  correspond to higher hygroscopicity and for atmospherically relevant particles  $\kappa$   
351 typically ranges from 0 to values exceeding 1. However, instead of a ratio of volumes mass-  
352 based growth factors can also be used to calculate  $\kappa$  by assuming particle density. A density-  
353 equivalent  $\kappa_{equiv}$ , which is defined as the  $\kappa$  value of a particle with the observed hygroscopic mass  
354 growth factor and assumed dry density,  $\rho_d$ , is calculated with equation 4:

$$355 \quad \kappa_{equiv} = (a_w^{-1} - 1)(g_m - 1)r \quad (4)$$

356 where  $r$  is the ratio of dry particle density to the density of pure water. Here we assume  $r = 1.760$   
357 based on the density of solid ammonium sulfate. Kelvin effects are neglected and water activity  
358 is taken to be the equilibrium RH. Density equivalent  $\kappa$  provides an approximate comparison to  
359 volume-growth factor published data in the literature.<sup>42-44</sup> If the studied particle density equals  
360 that of assumed value, the reported  $\kappa_{equiv}$  is identical to  $\kappa$  obtained via volumetric methods. A  
361 10% relative difference between actual and assumed particle density results in a 10% difference  
362 to values inferred from the volumetric-based method. The density equivalent  $\kappa_{equiv}$  values can be  
363 compared to the known  $\kappa$  values of other substances.<sup>42-44</sup> In this study, the most hygroscopic  
364 atmospheric particle observed has a density equivalent  $\kappa_{equiv}$  of 0.71 at high RH (80%), which is  
365 much lower than the estimated  $\kappa_{equiv}$  value reported for NaCl, but near the estimated  $\kappa_{equiv}$  values

366 for most sulfate and nitrate salts typically found in atmospheric aerosols.<sup>45</sup> Medium and low  
367 hygroscopicity particles have  $\kappa_{\text{equiv}}$  values in the same range as organic particles, attaining the  
368 lowest possible value of 0 for the low hygroscopicity particles.<sup>46</sup>

369 As described above, STXM/NEXAFS at the carbon K-edge identifies three components:  
370 organic (OC), inorganic (IN), and black carbon/soot (EC) to define a mixing state.<sup>37</sup> Figure S3 in  
371 the Supporting Information contains images that illustrate how the mixing state is determined for  
372 particles and Table S8 provides details on the mixing state classification. Figure 4 (left panel)  
373 shows the STXM based mixing states of the particles used for hygroscopic growth experiments  
374 (green) compared to that of the sample of 158 particles (blue). Based upon a visual analysis of  
375 preliminary STXM images we anticipated that these 15 particles were reasonably representative  
376 of the samples. Hence, they were selected for water vapor uptake experiments. Figure 4 (right  
377 panel) compares the size distribution of the 158 particles characterized using STXM/NEXAFS  
378 (blue) compared to that of the 15 particles selected for water vapor uptake experiments (green).  
379 Overall, the particle size distributions match well between the two sample sets. The agreement  
380 for the mixing state is lower (Figure 4, left panel) indicating that field samples containing more  
381 diverse particle-types would require better statistical depth. With the sample size of 15 particles,  
382 no significant correlation was found between hygroscopicity, and mixing state or particle size.  
383 However, if correlations were observed, by using a statistically significant subset of the  
384 population, then estimates for the hygroscopic behavior of the sample could be obtained.  
385 Additional characterization of the IN, via analysis with SEM/EDX, would be required as kappa  
386 values vary for different inorganic compounds.<sup>46</sup>

387 STXM/NEXAFS has previously been used to quantify the hygroscopicity of laboratory  
388 generated particles of known composition<sup>29,30,32,33</sup> and to observe the hygroscopic behavior of

389 ambient particles of unknown composition.<sup>21</sup> Here, we demonstrated that the combination of  
390 STXM/NEXAFS and SEM/EDX could quantitatively determine the hygroscopic behavior of  
391 both homogeneous particles with known composition and mixed atmospheric particles of  
392 unknown composition. Mass-based growth factors of mixed atmospheric particles of unknown  
393 composition were obtained on a per-particle basis by combining SEM/EDX measurements with  
394 STXM/NEXAFS characterizations. This method was validated using laboratory surrogates. Such  
395 data on field samples may provide means to correlate hygroscopic behavior and particle  
396 composition and chemistry. Although we attempted to find correlations between carbon  
397 functional groups (C=C, R-OH, COOH) and particle hygroscopicity, no apparent relationship  
398 was found. The mass-based growth factors can be used to characterize the statistics and range of  
399 hygroscopic behavior present in a sample of collected atmospheric particles and relate this range  
400 of behavior to elemental and functional chemistry.

401

## 402 **ASSOCIATED CONTENT**

### 403 **Supporting Information**

404 More detailed experimental methods for STXM/NEXAFS measurements and the  
405 characterization of SGP samples; the effects of uncertainty in nitrogen and silicon measurements  
406 on the mass-based growth factors of the SGP atmospheric particles; plot of size-based growth  
407 factors as a function of RH for the SGP atmospheric particles; tables containing the experimental  
408 data displayed in figures 1-4; images illustrating the mixing state of particles in terms of OC, EC  
409 and IN. This material is available free of charge via the Internet at <http://pubs.acs.org>.

## 410 **AUTHOR INFORMATION**

### 411 **Corresponding Authors**

412 \*E-mail: [dpiens@stanford.edu](mailto:dpiens@stanford.edu)

413 \*E-mail: [mkgilles@lbl.gov](mailto:mkgilles@lbl.gov)

#### 414 **ACKNOWLEDGEMENTS**

415 STXM/NEXAFS dry characterization experiments (MKG, STK, THH) were supported  
416 by the Atmospheric Systems Research (ASR) of the U.S. Department of Energy (DOE), Office  
417 of Science, Office of Biological and Environmental Research (OBER) program. Dry  
418 STXM/NEXAFS analysis of the field samples (THH) was partially supported by the German  
419 National Academic Foundation. Development of the MATLAB scripts and analysis for the mass-  
420 based water vapor uptake analysis (DSP) was supported through the DOE, Office of Workforce  
421 Development for Teachers and Scientists (WDTS) under the Science Undergraduate Laboratory  
422 Internship (SULI) program. REO (supported by DOE ASR) provided analysis guidance to both  
423 DSP and THH. The experimental portion of the water vapor uptake experiments (STK, MKG)  
424 and assistance with the interpretation of the data (MP) was supported by the ASR DOE OBER  
425 program. STXM/NEXAFS measurements were done with the assistance of Tolek Tyliczszak at  
426 Beamline 11.0.2 of the Advanced Light Source (ALS) at Lawrence Berkeley National  
427 Laboratory (LBNL). The ALS is supported by the Director, Office of Science, Office of Basic  
428 Energy Sciences (BES), of the U.S. DOE under Contract No. DE-AC02-05CH11231. Beamline  
429 11.0.2 is supported under the same contract as well as the Condensed Phase and Interfacial  
430 Molecular Sciences Program of DOE BES. AL and BW acknowledge support from support from  
431 the Chemical Imaging Initiative of the Laboratory Directed Research and Development program  
432 at Pacific Northwest National Laboratory (PNNL). The preparation of laboratory samples and  
433 SEM/EDX measurements were performed at the W. R. Wiley Environmental Molecular  
434 Sciences Laboratory (EMSL) - a national scientific user facility located at PNNL, and sponsored

435 by DOE OBER. PNNL is operated for US DOE by Battelle Memorial Institute under Contract  
436 No. DE-AC06-76RL0 1830. Samples were collected (KT, PD) at the Atmospheric Radiation  
437 Monitoring (ARM) site located at Southern Great Plains and sponsored by DOE OBER.

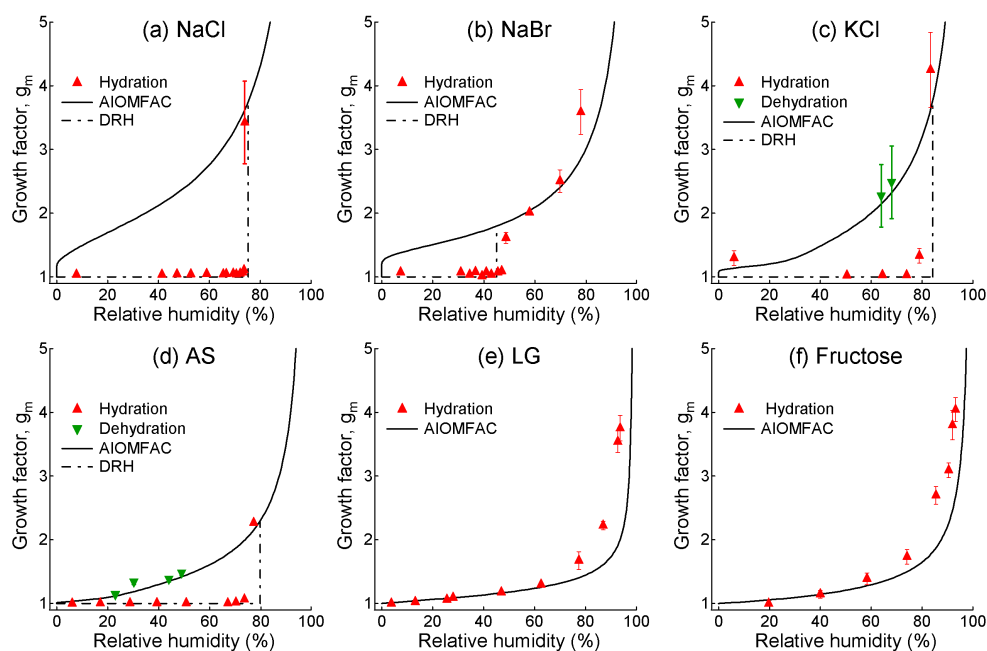
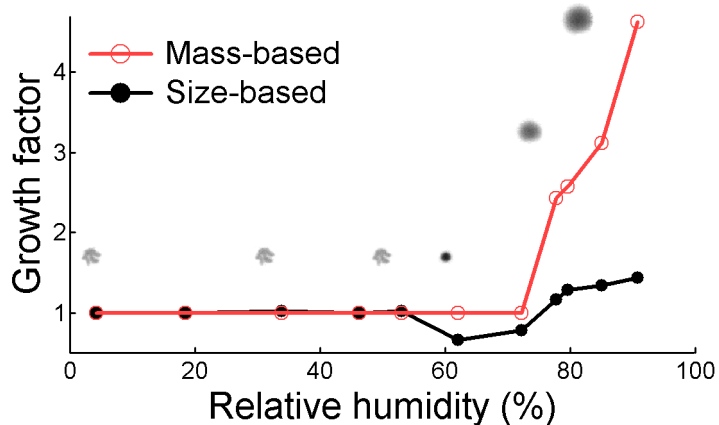


**Figure 1.** Experimental (red filled triangles) and AIOMFAC theoretical (black lines) mass-based growth factors as a function of relative humidity for (a) NaCl, (b) NaBr, (c) KCl, (d)  $(\text{NH}_4)_2\text{SO}_4$  labeled AS, (e) levoglucosan labeled LG, and (f) fructose. Dehydration data points are shown as green filled triangles. Deliquescence relative humidities (DRH) for NaCl and ammonium sulfate were obtained from Tang<sup>47</sup> and NaBr and KCl are from Cohen et al.<sup>41</sup> The error bars show the standard error of each point with sample sizes between two and six.

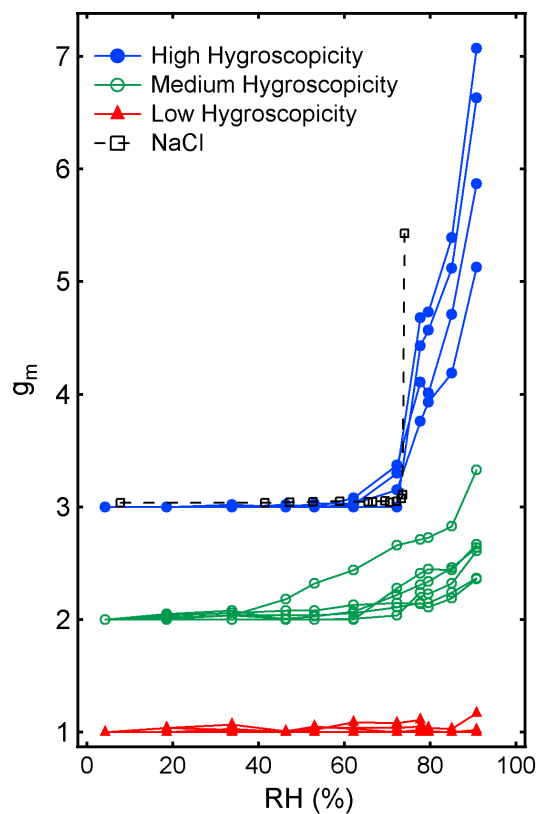


**Figure 2.** Mass-based growth factors of individual atmospheric particles (offset for clarity: by 1 for the green and 2 for the blue data points) grouped by their hygroscopic growth regime as a function of relative humidity. The water sorption isotherm of NaCl is overlaid on the water sorption isotherm of high hygroscopicity atmospheric aerosols.

Particle #	Hygroscopicity	$g_m$ (80% RH)	$K_{equiv}$ (80% RH)	Inorganic Atomic Fractions	4% RH	90% RH	Mixing State
1	High	2.73	0.71				OCIN
2	High	2.57	0.64				OCIN
3	High	2.01	0.41				OCECIN
4	High	1.93	0.38				OCIN
5	Medium	1.73	0.30				OCIN
6	Medium	1.45	0.18				OCECIN
7	Medium	1.34	0.14				OCIN
8	Medium	1.23	0.09				OCECIN
9	Medium	1.15	0.06				OCECIN
10	Medium	1.11	0.05				OCECIN
11	Low	1.04	0.02				OCECIN
12	Low	1.01	0.00				OCIN
13	Low	1.00	0.00				OCEC
14	Low	1.00	0.00				OCECIN
15	Low	1.00	0.00				OCECIN

0%      50%      100%      2  $\mu$ m

**Figure 3.** Table presenting hygroscopicity, mass-based growth factor at 80% RH ( $g_m$ ), hygroscopicity parameter  $\kappa_{equiv}$  at 80% RH, inorganic atomic composition, STXM images at 4% and 90% RH acquired at 525 eV, and mixing state classification for 15 atmospheric particles.



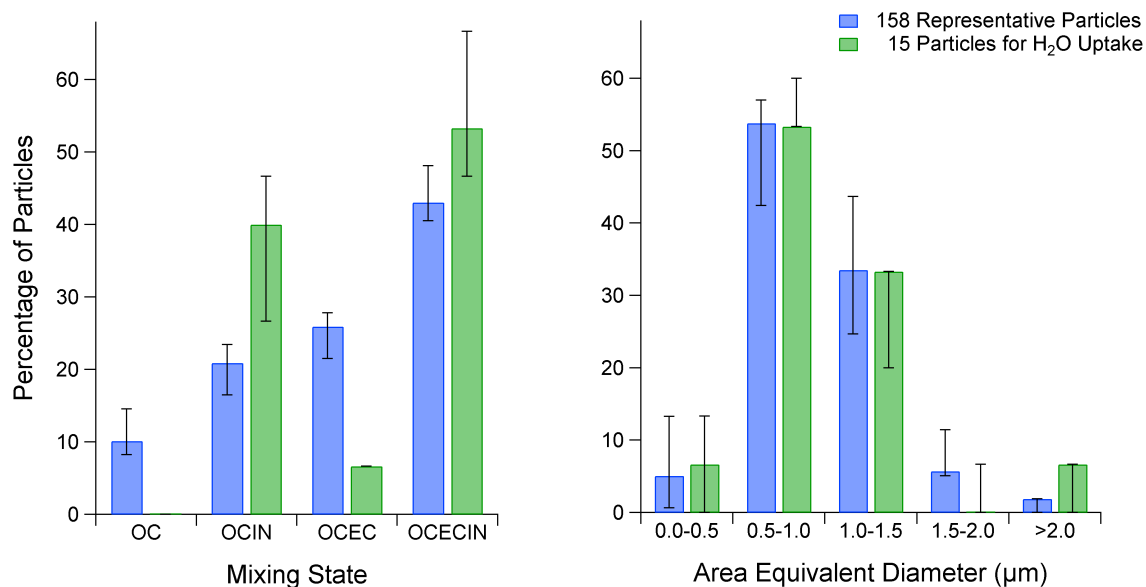


**Figure 4.** Left: STXM based mixing state distribution of all particles characterized on the Southern Great Plains sample (158) and the subset of the 15 particles used during water vapor uptake experiments. Mixtures of individual components (organic (OC), inorganic (IN), and black carbon/soot (EC)) within individual particles are indicated. Error bars calculated by varying the thresholds for classifying individual components by 10% are shown. Right: the corresponding size distributions. The error bars represent the change in size range frequencies due to an estimated uncertainty of  $\pm 2$  pixels on area equivalent diameter computation.

## REFERENCES

1. Andreae, M. O.; Rosenfeld, D., Aerosol-cloud-precipitation interactions. Part 1. The nature and sources of cloud-active aerosols. *Earth-Sci. Rev.* **2008**, *89*, (1-2), 13-41. DOI 10.1016/J.Earscirev.2008.03.001
2. Nguyen, T. K. V.; Petters, M. D.; Suda, S. R.; Guo, H.; Weber, R. J.; Carlton, A. G., Trends in particle-phase liquid water during the Southern Oxidant and Aerosol Study. *Atmos. Chem. Phys.* **2014**, *14*, (20), 10911-10930. DOI 10.5194/Acp-14-10911-2014
3. Swietlicki, E.; Hansson, H. C.; Hameri, K.; Svenningsson, B.; Massling, A.; McFiggans, G.; McMurry, P. H.; Petaja, T.; Tunved, P.; Gysel, M.; Topping, D.; Weingartner, E.; Baltensperger, U.; Rissler, J.; Wiedensohler, A.; Kulmala, M., Hygroscopic properties of submicrometer atmospheric aerosol particles measured with H-TDMA instruments in various environments - a review. *Tellus B* **2008**, *60*, (3), 432-469. DOI 10.1111/J.1600-0889.2008.00350.X
4. Suda, S. R.; Petters, M. D., Accurate determination of aerosol activity coefficients at relative humidities up to 99% using the hygroscopicity tandem differential mobility analyzer technique. *Aerosol. Sci. Tech.* **2013**, *47*, (9), 991-1000. DOI 10.1080/02786826.2013.807906
5. Yeung, M. C.; Lee, B. P.; Li, Y. J.; Chan, C. K., Simultaneous HTDMA and HR-ToF-AMS measurements at the HKUST Supersite in Hong Kong in 2011. *J. Geophys. Res.-Atmos.* **2014**, *119*, (16), 9864-9883. DOI 10.1002/2013jd021146
6. Martin, S. T.; Rosenoern, T.; Chen, Q.; Collins, D. R., Phase changes of ambient particles in the Southern Great Plains of Oklahoma. *Geophys. Res. Lett.* **2008**, *35*, (22), L22801. DOI 10.1029/2008GL035650
7. Liu, Y.; Laskin, A., Hygroscopic properties of  $\text{CH}_3\text{SO}_3\text{Na}$ ,  $\text{CH}_3\text{SO}_3\text{NH}_4$ ,  $(\text{CH}_3\text{SO}_3)_2\text{Mg}$ , and  $(\text{CH}_3\text{SO}_3)_2\text{Ca}$  particles studied by micro-FTIR spectroscopy. *J. Phys. Chem. A* **2009**, *113*, (8), 1531-1538. DOI 10.1021/Jp8079149
8. Liu, Y.; Yang, Z.; Desyaterik, Y.; Gassman, P. L.; Wang, H.; Laskin, A., Hygroscopic behavior of substrate-deposited particles studied by micro-FT-IR spectroscopy and complementary methods of particle analysis. *Anal. Chem.* **2008**, *80*, (3), 633-642. DOI 10.1021/Ac701638r
9. Ciobanu, V. G.; Marcolli, C.; Krieger, U. K.; Weers, U.; Peter, T., Liquid-liquid phase separation in mixed organic/inorganic aerosol particles. *J. Phys. Chem. A* **2009**, *113*, (41), 10966-10978. DOI 10.1021/jp905054d
10. Yeung, M. C.; Chan, C. K., Water content and phase transitions in particles of inorganic and organic species and their mixtures using micro-Raman spectroscopy. *Aerosol. Sci. Tech.* **2010**, *44*, (4), 269-280. DOI 10.1080/02786820903583786
11. Garland, R. M.; Wise, M. E.; Beaver, M. R.; DeWitt, H. L.; Aiken, A. C.; Jimenez, J. L.; Tolbert, M. A., Impact of palmitic acid coating on the water uptake and loss of ammonium sulfate particles. *Atmos. Chem. Phys.* **2005**, *5*, 1951-1961.
12. Laskina, O.; Morris, H. S.; Grandquist, J. R.; Qin, Z.; Stone, E. A.; Tivanski, A. V.; Grassian, V. H., Size matters in the water uptake and hygroscopic growth of atmospherically relevant multicomponent aerosol particles. *J. Phys. Chem. A* **2015**, *119*, (19), 4489-97. DOI 10.1021/jp510268p
13. Laskin, A., Electron beam analysis and microscopy of individual particles. In *Fundamentals and Applications in Aerosol Spectroscopy*, Signorell, R.; Reid, J. P., Eds. CRC Press Taylor & Francis: Boca Raton, FL., 2010; pp 463-491.

14. Posfai, M.; Buseck, P. R., Nature and climate effects of individual tropospheric aerosol particles. *Annu. Rev. Earth Pl. Sc.* **2010**, *38*, 17-43. DOI 10.1146/Annurev.Earth.031208.100032
15. Laskin, A.; Cowin, J. P.; Iedema, M. J., Analysis of individual environmental particles using modern methods of electron microscopy and X-ray microanalysis. *J. Electron Spectrosc. Relat. Phenom.* **2006**, *150*, (2-3), 260-274. DOI 10.1016/j.elspec.2005.06.008
16. Ahn, K. H.; Kim, S. M.; Jung, H. J.; Lee, M. J.; Eom, H. J.; Maskey, S.; Ro, C. U., Combined use of optical and electron microscopic techniques for the measurement of hygroscopic property, chemical composition, and morphology of individual aerosol particles. *Anal. Chem.* **2010**, *82*, (19), 7999-8009. 10.1021/ac101432y
17. Eom, H. J.; Gupta, D.; Li, X.; Jung, H. J.; Kim, H.; Ro, C. U., Influence of collecting substrates on the characterization of hygroscopic properties of inorganic aerosol particles. *Anal. Chem.* **2014**, *86*, (5), 2648-56. 10.1021/ac4042075
18. Wise, M. E.; Biskos, G.; Martin, S. T.; Russell, L. M.; Buseck, P. R., Phase transitions of single salt particles studied using a transmission electron microscope with an environmental cell. *Aerosol. Sci. Tech.* **2005**, *39*, (9), 849-856. DOI 10.1080/02786820500295263
19. Moffet, R. C.; Tivanski, A. V.; Gilles, M. K., Scanning transmission X-ray microscopy: Applications in atmospheric aerosol research. In *Fundamentals and Applications in Aerosol Spectroscopy*, Signorell, R.; Reid, J. P., Eds. CRC Press Taylor & Francis: Boca Raton, FL., 2010; pp 420-462.
20. Freney, E. J.; Martin, S. T.; Buseck, P. R., Deliquescence and efflorescence of potassium salts relevant to biomass-burning aerosol particles. *Aerosol. Sci. Tech.* **2009**, *43*, (8), 799-807. DOI 10.1080/02786820902946620
21. Pöhlker, C.; Saturno, J.; Kruger, M. L.; Forster, J. D.; Weigand, M.; Wiedemann, K. T.; Bechtel, M.; Artaxo, P.; Andreae, M. O., Efflorescence upon humidification? X-ray microspectroscopic in situ observation of changes in aerosol microstructure and phase state upon hydration. *Geophys. Res. Lett.* **2014**, *41*, (10), 3681-3689. DOI 10.1002/2014gl059409
22. Ghorai, S.; Wang, B. B.; Tivanski, A.; Laskin, A., Hygroscopic properties of internally mixed particles composed of NaCl and water-soluble organic acids. *Environ. Sci. Technol.* **2014**, *48*, (4), 2234-2241. DOI 10.1021/Es404727u
23. You, Y.; Renbaum-Wolff, L.; Carreras-Sospedra, M.; Hanna, S. J.; Hiranuma, N.; Kamal, S.; Smith, M. L.; Zhang, X. L.; Weber, R. J.; Shilling, J. E.; Dabdub, D.; Martin, S. T.; Bertram, A. K., Images reveal that atmospheric particles can undergo liquid-liquid phase separations. *Proc. Natl. Acad. Sci. U. S. A.* **2012**, *109*, (33), 13188-13193. DOI 10.1073/pnas.1206414109
24. You, Y.; Smith, M. L.; Song, M. J.; Martin, S. T.; Bertram, A. K., Liquid-liquid phase separation in atmospherically relevant particles consisting of organic species and inorganic salts. *Int. Rev. Phys. Chem.* **2014**, *33*, (1), 43-77. DOI 10.1080/0144235x.2014.890786
25. O'Brien, R. E.; Wang, B.; Kelly, S. T.; Lundt, N.; You, Y.; Bertram, A. K.; Laskin, A.; Gilles, M. K., Imaging of liquid-liquid phase separation in aerosol particles at nanometer scale. *Env. Sci. Technol.* **2015**, *49*, 4995-5002. DOI 10.1021/acs.est.5b00062
26. Tivanski, A. V.; Hopkins, R. J.; Tyliszczak, T.; Gilles, M. K., Oxygenated interface on biomass burn tar balls determined by single particle scanning transmission X-ray microscopy. *J. Phys. Chem. A.* **2007**, *111*, (25), 5448-5458. DOI 10.1021/Jp070155u
27. Hopkins, R. J.; Tivanski, A. V.; Marten, B. D.; Gilles, M. K., Chemical bonding and structure of black carbon reference materials and individual carbonaceous atmospheric aerosols. *J. Aerosol Sci.* **2007**, *38*, (6), 573-591. DOI 10.1016/j.jaerosci.2007.03.009

28. Maria, S. F.; Russell, L. M.; Gilles, M. K.; Myneni, S. C. B., Organic aerosol growth mechanisms and their climate-forcing implications. *Science* **2004**, *306*, (5703), 1921-1924. DOI 10.1126/Science.1103491
29. Ghorai, S.; Tivanski, A. V., Hygroscopic behavior of individual submicrometer particles studied by X-ray spectromicroscopy. *Anal. Chem.* **2010**, *82*, (22), 9289-9298. DOI 10.1021/Ac101797k
30. Kelly, S. T.; Nigge, P.; Prakash, S.; Laskin, A.; Wang, B.; Tyliszczak, T.; Leone, S. R.; Gilles, M. K., An environmental sample chamber for reliable scanning transmission X-ray microscopy measurements under water vapor. *Rev. Sci. Instrum.* **2013**, *84*, 073708. DOI 10.1063/1.4816649
31. Steimer, S. S.; Lampimaki, M.; Coz, E.; Grzanic, G.; Ammann, M., The influence of physical state on shikimic acid ozonolysis: A case for in situ microspectroscopy. *Atmos. Chem. Phys.* **2014**, *14*, (19), 10761-10772. DOI 10.5194/Acp-14-10761-2014
32. Zelenay, V.; Ammann, M.; Krepelova, A.; Birrer, M.; Tzvetkov, G.; Vernooij, M. G. C.; Raabe, J.; Huthwelker, T., Direct observation of water uptake and release in individual submicrometer sized ammonium sulfate and ammonium sulfate/adipic acid particles using X-ray microspectroscopy. *J. Aerosol Sci.* **2011**, *42*, (1), 38-51. DOI 10.1016/j.jaerosci.2010.11.001
33. Zelenay, V.; Huthwelker, T.; Krepelova, A.; Rudich, Y.; Ammann, M., Humidity driven nanoscale chemical separation in complex organic matter. *Environ. Chem.* **2011**, *8*, (4), 450-460. DOI 10.1071/En11047
34. Ghorai, S.; Laskin, A.; Tivanski, A. V., Spectroscopic evidence of keto-enol tautomerism in deliquesced malonic acid particles. *J. Phys. Chem. A.* **2011**, *115*, (17), 4373-4380. DOI 10.1021/Jp112360x
35. Mikhailov, E. F.; Mironov, G. N.; Pohlker, C.; Chi, X.; Kruger, M. L.; Shiraiwa, M.; Forster, J. D.; Poschl, U.; Vlasenko, S. S.; Ryshkevich, T. I.; Weigand, M.; Kilcoyne, A. L. D.; Andreae, M. O., Chemical composition, microstructure, and hygroscopic properties of aerosol particles at the Zotino Tall Tower Observatory (ZOTTO), Siberia, during a summer campaign. *Atmos. Chem. Phys.* **2015**, *15*, (15), 8847-8869. 10.5194/acp-15-8847-2015
36. Kilcoyne, A. L. D.; Tyliszczak, T.; Steele, W. F.; Fakra, S.; Hitchcock, P.; Franck, K.; Anderson, E.; Harteneck, B.; Rightor, E. G.; Mitchell, G. E.; Hitchcock, A. P.; Yang, L.; Warwick, T.; Ade, H., Interferometer-controlled scanning transmission X-ray microscopes at the Advanced Light Source. *J. Synchrotron. Radiat.* **2003**, *10*, 125-136. DOI 10.1107/S0909049502017739
37. Moffet, R. C.; Henn, T.; Laskin, A.; Gilles, M. K., Automated chemical analysis of internally mixed aerosol particles using X-ray spectromicroscopy at the carbon K-edge. *Anal. Chem.* **2010**, *82*, (19), 7906-7914. DOI 10.1021/Ac1012909
38. Henke, B. L.; Gullikson, E. M.; Davis, J. C., X-ray interactions -photoabsorption, scattering, transmission, and reflection at E=50-30,000 eV, Z=1-92. *Atom. Data Nucl. Data* **1993**, *54*, (2), 181-342. DOI 10.1006/Adnd.1993.1013
39. Zuend, A.; Marcolli, C.; Booth, A. M.; Lienhard, D. M.; Soonsin, V.; Krieger, U. K.; Topping, D. O.; McFiggans, G.; Peter, T.; Seinfeld, J. H., New and extended parameterization of the thermodynamic model AIOMFAC: calculation of activity coefficients for organic-inorganic mixtures containing carboxyl, hydroxyl, carbonyl, ether, ester, alkenyl, alkyl, and aromatic functional groups. *Atmos. Chem. Phys.* **2011**, *11*, (17), 9155-9206. Doi 10.5194/Acp-11-9155-2011

40. Zuend, A.; Marcolli, C.; Luo, B. P.; Peter, T., A thermodynamic model of mixed organic-inorganic aerosols to predict activity coefficients. *Atmos. Chem. Phys.* **2008**, *8*, (16), 4559-4593.
41. Cohen, M. D.; Flagan, R. C.; Seinfeld, J. H., Studies of concentrated electrolyte-solutions using the electrodynamic balance .3. Solute nucleation. *J. Phys. Chem.* **1987**, *91*, (17), 4583-4590. DOI 10.1021/J100301a031
42. Mikhailov, E.; Vlasenko, S.; Martin, S. T.; Koop, T.; Pöschl, U., Amorphous and crystalline aerosol particles interacting with water vapor: conceptual framework and experimental evidence for restructuring, phase transitions and kinetic limitations. *Atmos. Chem. Phys.* **2009**, *9*, (24), 9491-9522.
43. Mochida, M.; Kawamura, K., Hygroscopic properties of levoglucosan and related organic compounds characteristic to biomass burning aerosol particles. *J. Geophys. Res.-Atmos.* **2004**, *109*, (D21), D21202. DOI 10.1029/2004jd004962
44. Kramer, L.; Poschl, U.; Niessner, R., Microstructural rearrangement of sodium chloride condensation aerosol particles on interaction with water vapor. *J. Aerosol Sci.* **2000**, *31*, (6), 673-685. Doi 10.1016/S0021-8502(99)00551-0
45. Kreidenweis, S. M.; Petters, M. D.; DeMott, P. J., Single-parameter estimates of aerosol water content. *Environ. Res. Lett.* **2008**, *3*, (3), Artn 035002. Doi 10.1088/1748-9326/3/3/035002
46. Petters, M. D.; Kreidenweis, S. M., A single parameter representation of hygroscopic growth and cloud condensation nucleus activity. *Atmos. Chem. Phys.* **2007**, *7*, (8), 1961-1971.
47. Tang, I. N., Thermodynamic and optical properties of mixed-salt aerosols of atmospheric importance. *J. Geophys. Res.-Atmos.* **1997**, *102*, (D2), 1883-1893. DOI 10.1029/96jd03085